

pubs.acs.org/JACS Article

Heck Migratory Insertion Catalyzed by a Single Pt Atom Site

Bo Li, Cheng-Wei Ju, Wenlong Wang, Yanwei Gu, Shuai Chen, Yongrui Luo, Haozhe Zhang, Juan Yang, Hai-wei Liang, Mischa Bonn, Klaus Müllen,* William A. Goddard, III,* and Yazhou Zhou*



Cite This: J. Am. Chem. Soc. 2023, 145, 24126-24135



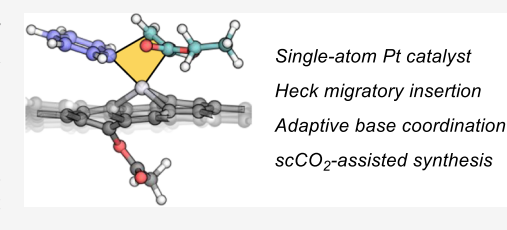
ACCESS I

III Metrics & More

Article Recommendations

Supporting Information

ABSTRACT: Single-atom catalysts (SACs) have generated excitement for their potential to downsize metal particles to the atomic limit with engineerable local environments and improved catalytic reactivities and selectivities. However, successes have been limited to small-molecule transformations with little progress toward targeting complex-building reactions, such as metal-catalyzed crosscoupling. Using a supercritical carbon-dioxide-assisted protocol, we report a heterogeneous single-atom Pt-catalyzed Heck reaction, which provides the first C-C bond-forming migratory insertion on SACs. Our quantum mechanical



computations establish the reaction mechanism to involve a novel C-rich coordination site (i.e., PtC₄) that demonstrates an unexpected base effect. Notably, the base was found to transiently modulate the coordination environment to allow migratory insertion into an M-C species, a process with a high steric impediment with no previous example on SACs. The studies showcase how SACs can introduce coordination structures that have remained underexplored in catalyst design. These findings offer immense potential for transferring the vast and highly versatile reaction manifold of migratory-insertion-based bond-forming protocols to heterogeneous SACs.

1. INTRODUCTION

Single-atom metal catalysts (SACs) have attracted wide attention in catalysis and energy research because they enable maximized metal utilization while introducing diverse and tailorable active sites. 1-4 Compared to conventional nanocatalysis, SACs both reduce the negative effects of hard-tocontrol physicochemical parameters such as local facets of nanoparticles and facilitate controlled modulation of the uncovered intrinsic active sites. 5,6 In principle, these atomically dispersed metal sites have clear coordination structures, giving rise to unique reaction pathways distinct from traditional heterogeneous catalysis. 7,8 The remarkable engineerability of SACs is complemented by many additional advantages such as high stability, lower preparation cost, and robustness toward harsh conditions.^{9,10}

The discovery of the most economical ways to construct C-C bonds has become increasingly significant for both industrial and academic research. With their unique and diverse reactivities, organometallic transition-metal catalysis has developed the foundation of modern organic synthetic methods, particularly in the construction of C-C bonds. 11-16 Notably, nearly all organometallic transitionmetal-catalyzed reactions comprise only a few elementary reactions such as oxidative addition, reductive elimination, transmetalation, migratory insertion, β -H elimination, metathesis, and hydrogen transfer (Figure 1a). For example, the Suzuki-Miyaura coupling, 17 one of the most powerful reactions in the pharmaceutical chemist armory, comprises oxidative addition, transmetalation, and reductive elimination. Similarly, the consecutive sequence of oxidative addition,

migratory insertion, and β -H elimination gives rise to the Heck reaction, 18 the discovery of which shared the 2010 Nobel prize. The Heck reaction is involved in countless applications in the medical, pharmaceutical, and electronics industries, 13,14,19-24 not only for organic synthesis but also for novel reaction-based functionalities such as human genome mapping by coupling fluorescent dyes with DNA strands. Nowadays, expedited access to complex molecules is being increasingly achieved by new methods with purposeful combination and programming over the toolkit of known elementary reactions to improve the economics, efficacy, and yields in both experimental laboratories and industry. Therefore, the implementation of diverse elementary reactions is of primary significance for any transition-metal-centered catalyst. This is clearly mirrored by, for example, the rapid diversification of iron-metalloenzymecatalyzed reactions in recent years as their reactivity modes have expanded toward carbene-based and other functionalities.²⁵⁻²⁸ For the SAC counterparts, however, nearly all transition-metal-catalyzed C-C bond-forming methods have remained limited to Suzuki-Miyaura coupling and reactions with similar mechanisms. 29,30

We argue that further expansion of elementary reactions can offer great opportunities for numerous organic reactions

Received: July 23, 2023 Revised: October 10, 2023 Accepted: October 11, 2023 Published: October 23, 2023





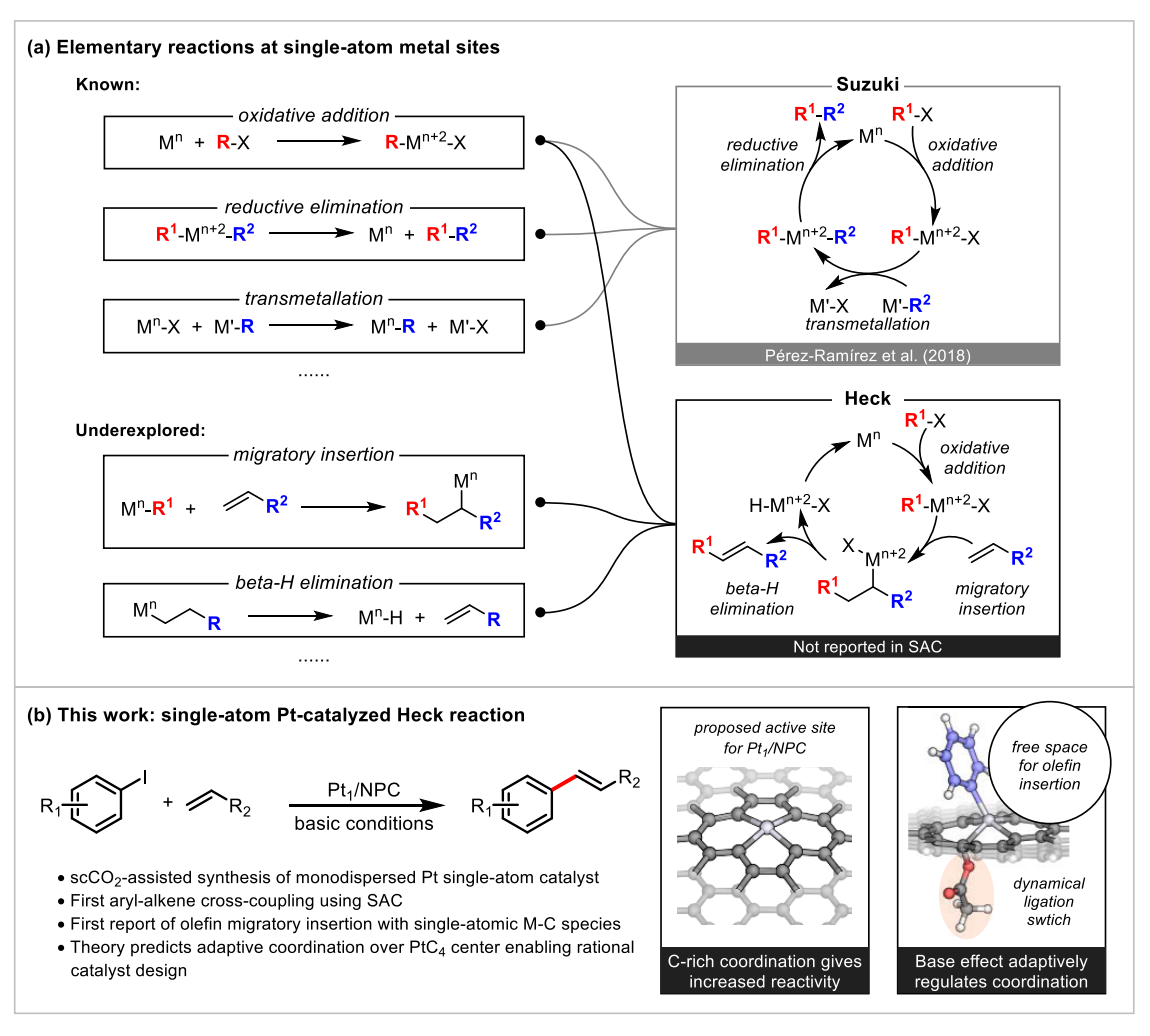


Figure 1. Introduction. (a) Known and unexplored elementary reactions at single-atom metal sites, demonstrating how programmable arrays of elementary reactions (left) give rise to the Suzuki and Heck reactions (right). (b) This work: single-atom Pt-catalyzed Heck reaction (left) and a plausible mechanistic model (right) featuring C-rich coordination and base-promoted adaptive coordination, which enables an in situ steric tuning to allow the olefinic insertion.

currently inaccessible for SACs, especially the lack of migratory insertion, given its pivotal role in C–C bond construction. ^{29–31} However, migratory insertion into a single-atom M– C bond is greatly challenged by the substantial steric demand, as two sizable organic moieties are joined together in an innersphere fashion. This can hardly be accommodated by metal atoms embedded on a solid surface. Moreover, M-C bonding is usually highly localized and directional because the sp^{n} hybridized C orbital is strictly oriented toward the metal center, which hampers effective orbital interactions with the inserting partner. Strategic catalytic design for resolving these multifaceted challenges has yet to be achieved.

Here, we report the first Heck reaction with SACs, providing the first realization of an olefinic migratory insertion (Figure 1b). In order to improve the density of Pt sites, we developed a supercritical carbon dioxide (scCO₂)-assisted protocol to uniformly disperse platinum acetylacetonate (Pt(acac)₂) on carbon supports, including nitrogen-doped porous carbon and activated carbon, followed by thermal reduction. Extensive quantum mechanics modeling of the atomistic catalytic process in tandem with experimental validation implicates a novel Crich coordination environment for the Pt site. We propose that in the presence of acetate base, the PtC₄-type active site can

transiently generate a unique PtC₃/C-OAc-type structure that significantly lowers the steric impediment to olefin insertion. This rare report on C-rich metal coordination in the SAC field highlights how coordination regulation at heterogeneous single-atom sites can offer classically inaccessible catalytic units to expand the reaction manifold of SACs.

2. RESULTS

2.1. Synthesis and Characterization of the Catalysts.

The wet impregnation method is often carried out for the preparation of SACs.³² Poor dispersion and high interfacial tension of solid supports in the solvent limit the uniform distribution of the metal precursors. This increases the likelihood of the sintering of metals to a varied population of nanostructures, including atomic species, clusters, and nanoparticles.^{33–35} Toward this end, we demonstrated the scCO₂assisted method to highly disperse Pt atoms on nitrogen-doped porous carbon (denoted as Pt₁/NPC). The fabrication process is illustrated in Figure 2a. Pt(acac)₂ molecules were completely dissolved into scCO2 to form a single phase at 65 °C and 10 MPa. Due to its low viscosity, zero surface tension, and high diffusivity, 36-39 gas-like scCO2 delivered Pt(acac)2 to any location on the carbon particles, leading to a uniform

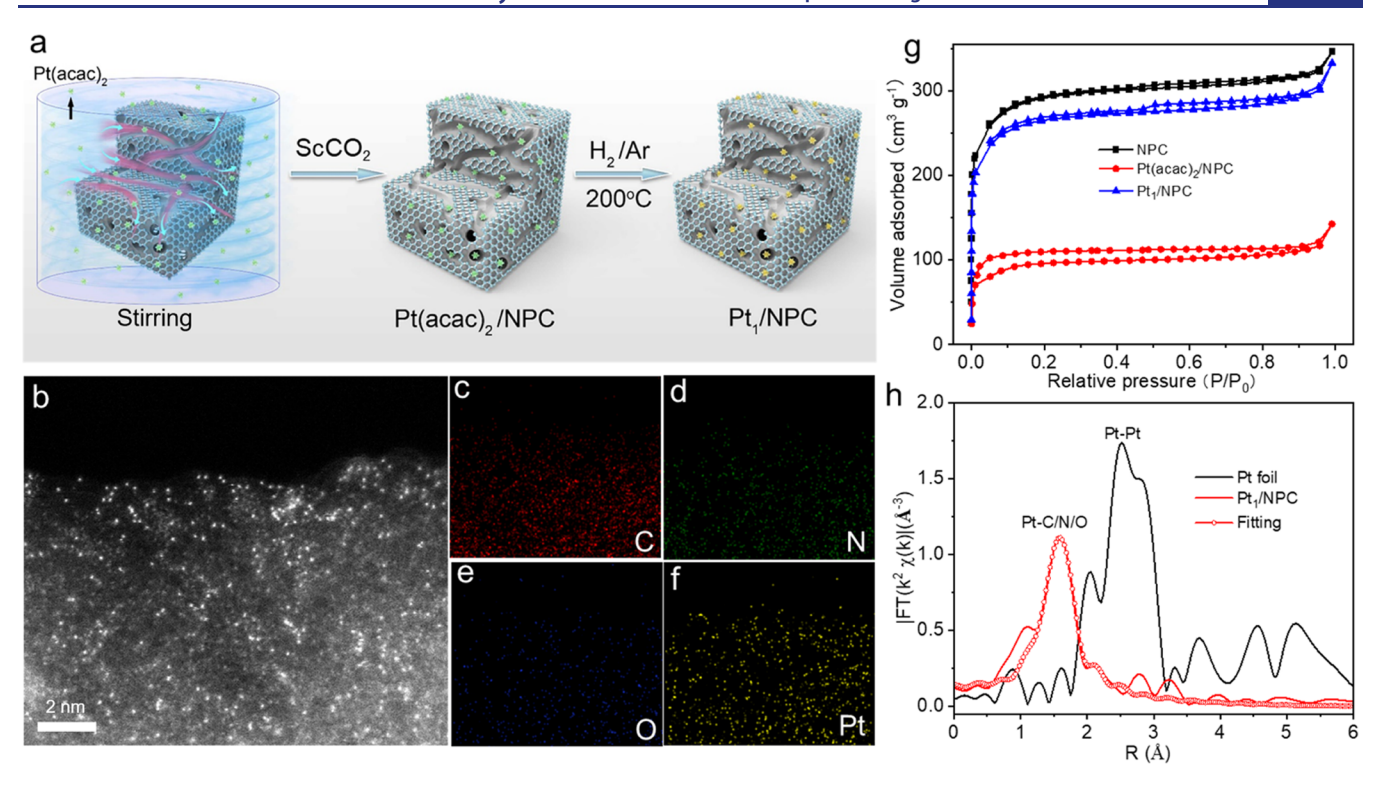


Figure 2. Preparation and characterization of Pt_1/NPC . (a) Schematic illustration of the $scCO_2$ -assisted method for Pt_1/NPC synthesis, (b) aberration-corrected HAADF-STEM image of Pt_1/NPC with elemental mappings of (c), C, (d), N, (e), O, and (f), Pt. Scale bar in (b) is 2 nm. (g) N_2 adsorption—desorption isotherms of NPC, $Pt(acac)_2/NPC$, and Pt_1/NPC . (h) Pt K-edge Fourier transform EXAFS of Pt_1/NPC with reference material of Pt foil, and its fit of Pt_1/NPC .

distribution (denoted as $Pt(acac)_2/NPC$). Finally, the Pt_1/NPC catalyst was obtained by a thermal reduction with 10 vol % H_2/Ar at 200 °C.

NPC supports with abundant defects were prepared using pyrolyzed zeolitic imidazolate frameworks (ZIF-8) (see the Section 4) and characterized by X-ray diffraction (XRD), transmission electron microscopy (TEM), Raman spectroscopy, and X-ray photoelectron spectroscopy (XPS) (Figures S1 and S2). The high-intensity ratio of the D (ca. 1342 cm^{-1}) and G (ca. 1586 cm⁻¹) bands indicates the high density of defects in NPC supports 40 (Figure S2a). The high-resolution N 1s XPS spectrum revealed the presence of four types of N species, namely, pyridinic N (398.6 eV), pyrrolic N (399.7 eV), graphitic N (401.0 eV), and oxidized N (402.3 eV) (Figure S2b).⁴¹ The introduction of N-doping during the hightemperature pyrolysis process leads to the formation of various defects, including nitrogen divacancy, carbon vacancy, edgesite defects, and topological defects. 42 Aberration-corrected high-angle annular dark-field scanning transmission electron microscopy (HAADF-STEM) showed numerous individual bright dots that correspond to single Pt atoms on the surface of the NPC supports (Figure 2b). Electron energy loss spectroscopy (EELS) maps of the Pt₁/NPC catalyst established that C, N, O, and Pt were evenly dispersed throughout the carbon layers (Figure 2c-f). Characterization of the material by XRD, TEM, and high-resolution TEM suggested the absence of Pt aggregates (Figures S3 and S4). The content of Pt in the Pt₁/ NPC sample was examined by inductively coupled plasma optical emission spectrometry (ICP-OES) and found to be 4 wt %. As the Pt loading increased (up to 6 wt %), the sample displayed the coexistence of individual atoms and clusters with an average size of ~1.2 nm (labeled as Pt₁/Ptcs/NPC)

(Figures S3, S5, and S6). In contrast, Pt nanoparticles on NPC (Pt NP/NPC) were obtained by using the wet impregnation method with the same amount of Pt(acac)₂ (Figures S3, S7, and S8). The superiority of the scCO₂-assisted approach over the wet impregnation method was demonstrated by Brunauer-Emmett-Teller (BET) surface area analysis. The NPC supports display abundant supermicopores (<1 nm), attributed to the cavities. 42 The BET surface area of NPC supports decreased significantly after the adsorption of Pt(acac)2 molecules in the scCO2 environment. After the thermal reduction process, the resulting Pt₁/NPC exhibited nearly the same BET surface area as the NPC supports (Figures 2g and S9b). The high BET surface area (853 m² g⁻¹) and porous structures (Table S1) indicate excellent accessibility of the Pt atoms. In contrast, the low BET surface areas of samples prepared with the wet impregnation method indicate that poor dispersion of Pt(acac), molecules on the support may be the main reason for the formation of Pt nanoparticles rather than single atoms (Figure S9c,d). Additionally, this scCO₂-assisted method avoids the use of large amounts of organic solvents and drying processes, making it both economical and environmentally friendly.

XPS analysis demonstrated a peak position of the Pt $(4f_{7/2})$ between those of Pt(II) and Pt(0), confirming that Pt(acac)₂ molecules were reduced by H₂ (Figure S10). No obvious Pt—O XPS signal was detected. X-ray absorption near-edge structure (XANES) indicates that the white line intensity of the Pt₁/NPC was between that of Pt foil and PtO₂, suggesting the partial oxidation state of Pt (Figure S11), which is consistent with the XPS result. The Fourier transforms of the extended X-ray absorption fine structure (EXAFS) analysis (Figure 2h) presented an intense peak at approximately 1.58 Å,

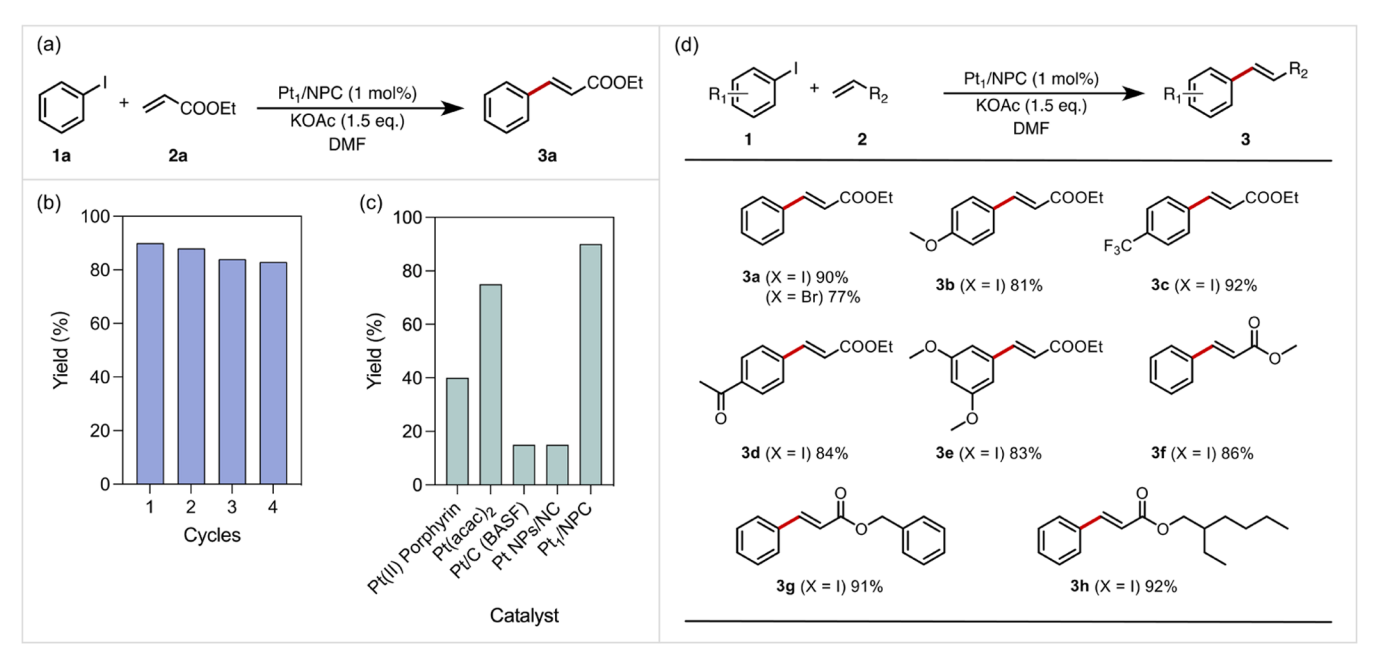


Figure 3. Heck reaction performance. (a) Reaction scheme for the Heck reaction. The reaction was run with iodobenzene 1a (1.0 equiv), ethyl acrylate 2a (1.3 equiv), Pt₁/NPC catalyst (1 mol %), and KOAc (1.5 equiv) in DMF (0.5 mol) at 125 °C for 24 h under a nitrogen atmosphere. Yields shown in this figure were determined by ¹H NMR analysis using dibromomethane as an internal standard. (b) Recycle performance of Pt₁/NPC catalyst. (c) Catalytic activity of Pt₁/NPC and various Pt-based heterogeneous and homogeneous catalysts of Pt NPs/NPC, Pt/C (2–3 nm, BASF), Pt(II) Porphyrin, and Pt(acac)₂. (d) Catalytic activity with various bases.

which corresponds to Pt–C/N/O coordination. The absence of a Pt–Pt scattering peak at the position of 2.76 Å is consistent with the detailed wavelet transform (WT) EXAFS (WT-EXAFS). These results confirm that single-atom Pt sites dominate the Pt₁/NPC (Figure S12). Due to various anchoring sites in NPC supports, possible single-site structures of Pt have Pt–C/N/O coordination. The EXAFS results lead to a best fit of 3.9 \pm 0.3 for the coordination number of the first-coordination sphere with a distance of 1.98 \pm 0.01 Å (Figure 2h and Table S2).

2.2. Heck Reaction Performance. To evaluate the reactivity of Pt₁/NPC in migratory insertion, we chose a well-known organic reaction, the Heck reaction, as a model (Figure 3a). To demonstrate the improvement brought about by SACs, we use Pt rather than Pd-based catalysts due to the relatively low reactivity of Pt in homogeneous catalysts. However, this choice faces several formidable challenges: (i) oxidative addition to a tetracoordinate Pt(0) species (18 e⁻ structure) at the PtC₄ center is quite difficult (oxidative addition is usually initiated by a bis-coordinated Pt(0) complex with a 14 e⁻ structure); (ii) halogen dissociation of the Pt(II) oxidative addition intermediates may be slower than that of Pd(II) analogs, which hampers the olefin-Pt interaction; (iii) alkene insertion in a congested Pt(II) intermediate is kinetically unfavorable; and (iv) reductive elimination of Pt(II)-H species with a base to regenerate the active Pt(0) state is much more difficult than its Pd counterpart.

To our satisfaction, the Pt_1/NPC catalyst displays remarkably high activity with a 91% yield (determined by 1H NMR) for the reaction between iodobenzene and ethyl acrylate (Figure 3a). After four recycles, more than 90% activity with a yield up to 83% was retained, also indicating high recyclability (Figure 3b). The used catalyst was again characterized using TEM, high-resolution TEM, STEM, aberration-corrected HAADF-STEM, and elemental mappings

(Figures S13–S15). These combined results affirm the stability of Pt_1/NPC under the conditions of the Heck reaction. The comparison with Pt NPs and Pt cluster catalysts highlights the advantage of downsizing Pt NPs on the support to create SACs with improved reactivity (only ~20% yield for Pt NPs/NPC and commercial Pt/C catalysts and 75% for $Pt_1/Ptcs/NPC$) (Figure 3c). Next, we compared the activity between Pt_1/NPC and Pt-based homogeneous catalysts including $Pt(acac)_2$ and Pt(II)-porphyrin. These results showed that a 78% yield can be achieved on $Pt(acac)_2$ against only 40% for Pt(II)-porphyrin. The low performance of Pt(II)-porphyrin indicates that a $Pt-N_4$ configuration is likely not an active structure for this reaction.

Next, to further validate the catalytic activity of Pt₁/NPC on various substrates, we investigated the reactant scope under the optimized reaction conditions at 125 °C (Figure 3d). These results revealed that Pt₁/NPC catalyzes the Heck reaction experimentally not only for different aryl iodides but also for aryl bromides with alkenes in the presence of KOAc(3a). Both electron-withdrawing and electron-rich functional groupsubstituted aryl iodides react well with ethyl acrylate to produce the coupled products 3b-3d with high yields (>80%). Meta-disubstituted aryl iodide also furnishes a high yield (3e). Furthermore, diverse acrylates can be smoothly converted into the corresponding products 3f-3h, including the industrially produced ultraviolet (UV)-protecting agent cinnamyl 3h. Moreover, a promising >80% yield was obtained when scaled up to use 20 mmol of iodobenzene and 0.5 mol % of Pt₁/NPC. Thus, the high catalytic activity of Pt₁/NPC in various organic metal reactions and large-scale reaction conditions demonstrates the great potential of SACs for applications in realworld problems of pharmaceutical production.

2.3. Theoretical Studies. After establishing the single-atom Pt-catalyzed Heck reaction, we questioned the origin of such reactivity and its implications for migratory insertion. To

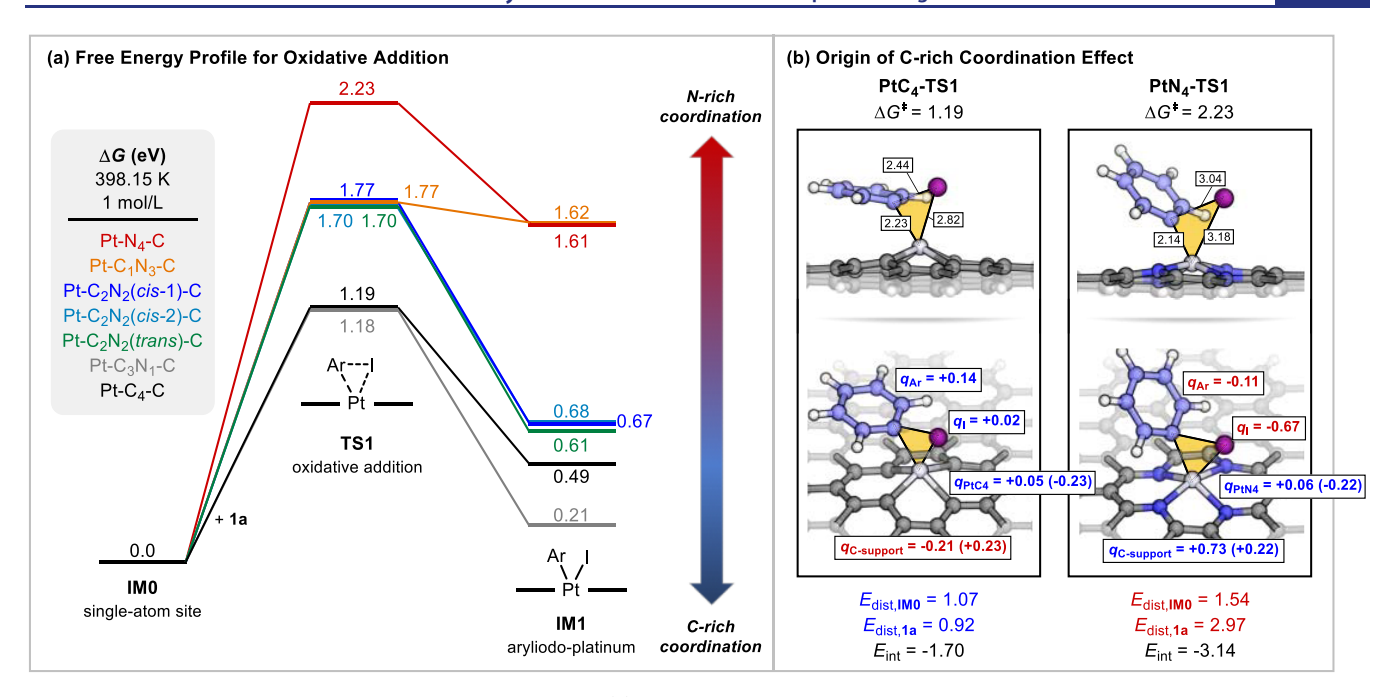


Figure 4. Effect of C-rich coordination on oxidative addition. (a) Free-energy profiles for possible inner-sphere coordination modes, showcasing the lower activation barrier at C-rich Pt centers. (b) Transition state structures with Hirshfeld charge populations⁴³ and distortion/interaction energies⁴⁴ reveal stretched and charge-separated characters for the PtN₄ site, explaining the preferential C-rich coordination. Partial charges at the reactant state are presented in parentheses and are analogous for the two sites. All free energies are in eV and distances in Å.

this end, we employed quantum mechanical (QM) calculations to investigate the possible catalytic mechanisms for a singleatom Pt site. Based on the XPS and EXAFS analysis, we considered PtC_xN_{4-x} (x = 0-4) models as possible Pt sites. Our results indicate that the SAC catalyst relies on a C-rich coordination, and we find that an unanticipated acetate-based dynamical coordination regulation can promote the migratory insertion through lowering the activation barrier by a notable ~0.4 eV.

2.3.1. Effect of C-Rich Coordination. Following the standard Heck pathway, we postulated that the catalysis is initiated by the oxidative addition of the reactive $C(sp^2)$ -I bond in 1a, furnishing aryliodoplatinum species IM1 via transition state TS1. As presented in Figure 4a, the energetics of this process heavily depend on the ligating atoms, strongly favoring C-rich coordination. Thus, the activation energies for PtC₄-TS1 and PtC₃N₁-TS1 are plausible ($\Delta G^{\ddagger} \sim 1.2 \text{ eV}$), whereas oxidative additions via PtN₄-/PtC₁N₃-/PtC₂N₂-TS1 exhibit prohibitively high barriers ($\Delta G^{\ddagger} \geq 1.7$ eV). The formation energies of resultant IM1 follow a similar trend of favoring C-rich centers.

We analyzed the origin of the C-rich coordination. Shown in Figure 4b is a composite geometric/charge-population analysis for PtC4-TS1 and PtN4-TS1. While PtC4-TS1 supports concerted character with reasonable interatomic distances and close-to-neutral partial charges at the Pt/Ar-I reaction center, PtN₄-TS1 presents strong nonconcerted features with an exceptionally stretched $C(sp^2)$ -I bond (3.04 Å) and an elongated Pt-I distance (3.18 Å). These values are associated with a rather negatively charged iodine $(q_I = -0.67)$, ⁴³ manifesting features of a partially dissociative closed-shell I-, which becomes unfavorable to further bonding. In accordance with our observations, distortion/interaction analysis, 44 which partitions the activation energy into

(a) distortion energies (E_{dist}) for the individual reactants and

(b) interaction energy (E_{int}) between the distorted (thus prepared) reactants,

yields a high substrate distortion energy in PtN₄-TS1 $(E_{\text{dist},1a}(\text{PtN}_4\text{-TS1}) \text{ of } 2.97 \text{ eV } vs \ E_{\text{dist},1a}(\text{PtC}_4\text{-TS1}) = 0.92 \text{ eV}).$ Notably, despite contrasting patterns of charge redistribution at TS1, the PtC4 and PtN4 sites exhibit similar charges for the reactant state (see values in parentheses). Meanwhile, calculations of intrinsic bond orbitals 45,46 along the reaction path show that the expected $d_{22}(Pt) \rightarrow aryl$ and $\sigma(aryl-I) \rightarrow$ Pt electron flows of oxidative addition occur on both sites (Figure S16). We thus ascribe the coordination effect to the distinct trends of charge redistribution accompanying oxidative addition, rendering PtN₄ to be much more repulsive than PtC₄ in TS1.

In addition to the electronic effect, the PtC4 center more readily undergoes out-of-plane structural distortion, which is seen in Figure 4b from the side-view display and the lower distortion energies $(E_{\text{dist},\text{IM0}}(\text{PtC}_4\text{-TS1}) = 1.07 \text{ eV} <$ $E_{\text{dist.IM0}}(\text{PtN}_4\text{-TS1})$ 1.54 eV, see Figure S17 for scanned distortion profiles). This also contributes to the preference for C-ligation.

In addition, Figure 4a suggests a violation of the general trend in the sense that PtC₃N₁ shows a lower intermediate energy than PtN₄. Based on an analysis of the intermediate structures, we tentatively hypothesize that the introduction of a single N atom in the PtC₃N₁ site enables more geometric relaxations that minimize electronic destabilization (Figure S18).

We also examined oxidative addition for the Pt-P homogeneous catalyst. Likely for similar reasons, the additions of 1a to the N₄-coordinated Pt exhibit a prohibitively high barrier (2.44-2.64 eV, see Figure S19). Given the ubiquity of M-N₄-type active sites in many domains of catalysis, our model highlights that the underexplored C-rich coordination can form a new basis for the rational engineering of transition-

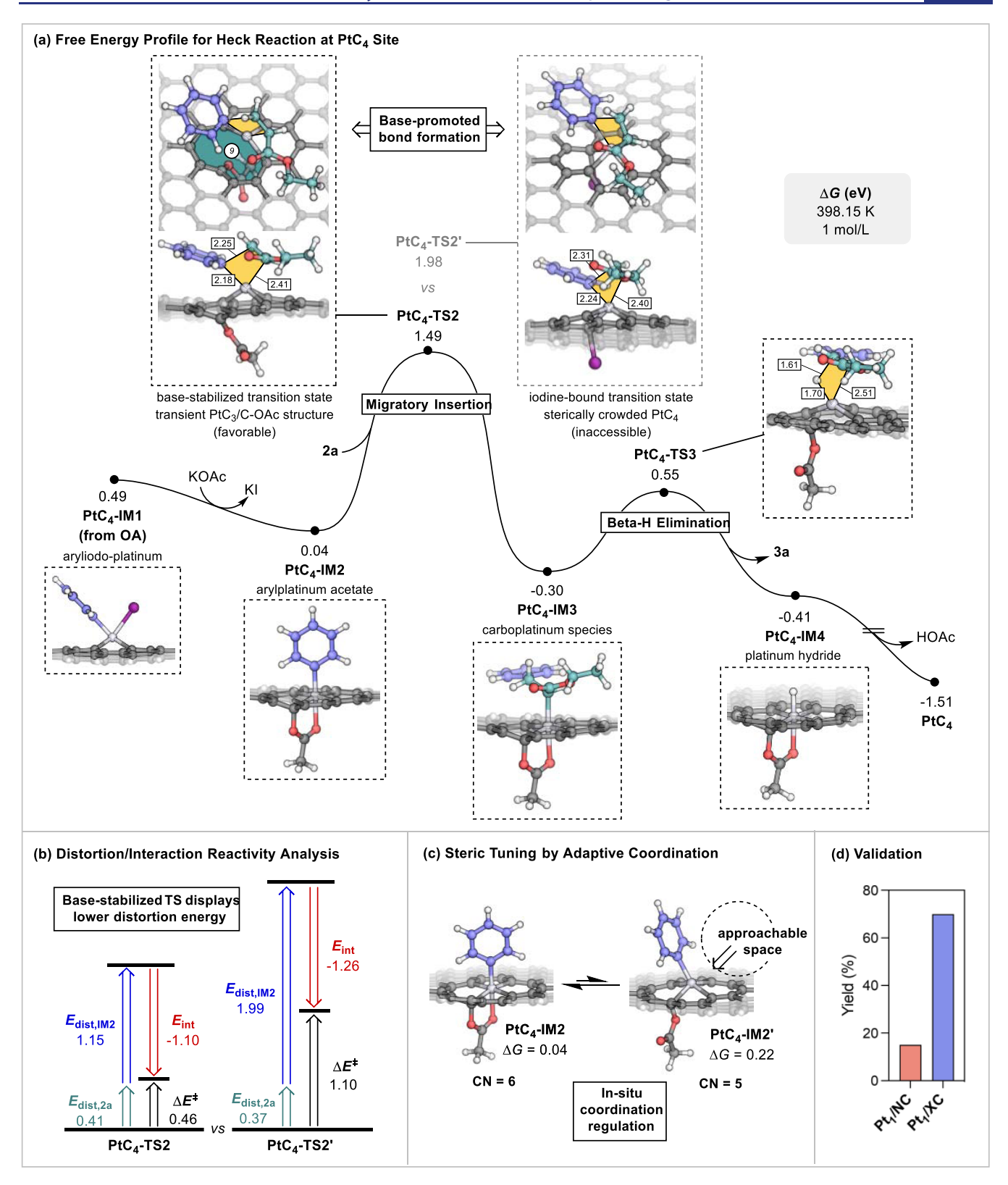


Figure 5. Base effect on C–C bond formation. (a) Free-energy profile for the PtC₄ site continuing from Figure 4a, showing that olefin insertion is the rate-limiting step and that AcO⁻ transiently breaks a Pt–C bond to provide a fleeting PtC₃/C–OAc structure in the transition state PtC₄-TS2. This adaptive ligation dramatically lowers the activation barrier of PtC₄-TS2 compared with that of the iodine-bound counterpart PtC₄-TS2′. All free energies are in eV, distances in Å. (b) Distortion/interaction reactivity analysis for the two above-mentioned transition states, suggesting distortion control of olefin insertion. (c) Steric tuning, as indicated by the structural prearrangement prior to olefin insertion, supports the proposed in situ coordination regulation. (d) Reaction yields when different base reagents are used instead of KOAc. All carbonates led to no observable reaction. Other conditions strictly follow the standard one described in Figure 3.

metal reactivity applicable beyond single-atom catalysis. Further validation is presented later to strengthen our hypothesis.

2.3.2. Base-Promoted Dynamical Coordination Regulation. To establish a model for bond formation, we next explored the entire Heck pathway using PtC4 as a representative structure. We note that other Pt sites show almost parallel energy profiles in the following steps, albeit the differential oxidative addition energies render C-rich coordination overall lower in energy (Figure S20). As displayed in Figure 5a, anti-displacement of the oxidative adduct PtC₄-IM1 with KOAc can occur to furnish PtC4-IM2. This is exergonic because the dual Pt-I and Pt-Ar bonds of PtC4-IM1 on the same side of the metal build up a high strain. Thereafter, I^-/I AcO exchange can spontaneously give PtC₄-IM2, which has a more stable octahedral coordination, to effectively release the strain. Notably, these structural relaxations predict that, besides the anticipated axial binding, AcO is covalently attached to a ligating C neighbor. A five-membered chelate ring is thereby formed that can be carried over for the following intermediates. Subsequent elementary steps include olefin insertion with Pt-Ar species (IM2 + 2a \rightarrow IM3), β -H elimination to generate the coupling product (IM3 \rightarrow IM4 + 3a), and reductive elimination to reinstitute the Pt site.

Our main interest in this study lies in the olefin insertion in SACs, which constitutes the rate-limiting step, as anticipated. Unexpectedly, we found a critical base effect on C-C bond formation. The insertion is viable only in the presence of AcO⁻, namely, via PtC₄-TS2 ($\Delta G^{\ddagger} = 1.49$ eV). For comparison, the iodine-bound form PtC4-TS2' exhibits an elevated barrier ($\Delta G^{\ddagger} = 1.98 \text{ eV}$). Inspection of the transition states suggests a transient interruption of Pt-C bonding in PtC₄-TS2, forming a unique PtC₃/C-OAc site, wherein Pt becomes more accessible. We postulate that the sterically crowded M-C olefin insertion can be better accommodated because of this in situ coordination regulation. 47-50

We then examined our hypothesis with combined energetic/ structural analysis. As an energetic probe, distortion/ interaction analysis⁴⁴ identified dramatically lower arylplatinum distortion energy ($E_{\text{dist,IM2}}$) in the base-stabilized PtC₄-TS2 (1.15 eV) than in the iodine-bound PtC_4 -TS2' (1.99 eV, notice that $E_{\text{dist},2a}$ and E_{int} are largely consistent, see Figure 5b) (note: a distortion/interaction analysis on transition state models with reduced size gave consistent results, see Table S3). To delineate the dynamic process of how AcO⁻ tailors the Pt site, we then explored the preparatory coordination regulation prior to PtC₄-TS2. As depicted in Figure 5c, AcO can readily predissociate from Pt while remaining attached to the C neighbor ($\Delta G = 0.22$ eV). The resultant pentacoordinate arylplatinum PtC₄-IM2' features a perturbed aryl positioning. This prearranged structure exposes a considerably more approachable Pt-Ar than the octahedrally coordinated PtC4-IM2, thus facilitating the desired olefin insertion. This prearranged site can then transiently undergo Pt-C bond cleavage during insertion to form the PtC₃/C-OAc structure in PtC_4 -TS2.

To further support our computational insight, we validated our hypothesis that the effect of C-rich coordination can promote the Heck reaction by the occurrence of C-rich and Nrich SAC. The Pt₁/NC was synthesized using the NC with a high amount of N doping (9 at%), while the Pt₁/XC-72 was prepared using commercial carbon black (Vulcan XC-72) activated carbon. The superiority of Pt₁/XC-72 demonstrated

a ~5-fold yield increase, reaching 75% (Figure 5d), validating our above hypothesis. Further improving the activity of Pt₁/ XC-72, requires increasing the Pt density, which remains a challenge due to the low density of defects for hosting Pt sites on activated carbon.

We note that the current modeling does not fully capture the complexity of the secondary catalytic environment and its broader context. While we believe that our modeling offers valid insights into the dominant coordination site, further investigations may be needed to understand fully the largerscale heterogeneous environmental effects that might play a role in the catalytic process.

3. CONCLUSIONS

We described a novel heterogeneous single-atom Pt-catalyzed Heck reaction. Using a scCO₂-assisted protocol, the resulting Pt SAC achieved excellent activity, robust recyclability, and good functional group tolerance. Our quantum mechanics computations established a unique mechanism of catalysis in which the single-atom site possesses a reactive C-rich coordination mode. These analyses highlight the merits of SACs as useful platforms for studying underexplored coordination structures for transition-metal catalysis. Most surprisingly, base-assisted adaptive coordination regulation facilitates bond-forming migratory insertion, greatly reducing the otherwise prohibitively large steric impediment for the approaching olefin. Indeed, our work represents the first realization of migratory insertion into single-atom-site M-C species. The strategies and principles implicated are expected to offer ample opportunities for heterogeneous SACs to advance toward the vast space of migratory-insertion-based complexity-building reactions, which hold great potential for efficient synthetic access to value-added molecular products.

4. METHODS

4.1. Synthesis of NPC and N-Rich NC Supports. A 15 mL methanol solution containing 0.513 g of zinc nitrate hexahydrate was mixed with another 15 mL of 2-methylimidazole (0.577 g) methanol solution. The mixture solution was loaded into an autoclave and then placed in an oven at 120 °C for 4 h. The ZIF-8 suspension was collected, washed with methanol several times, and then dried at 60 °C in a vacuum oven overnight. The ZIF-8 powders were pyrolyzed at 950 °C for 3 h under an Ar atmosphere, followed by washing with 2 M HCl solution at 80 °C overnight to remove Zn species and drying at 80 °C in a vacuum oven. The obtained product with N content of 3.5 atom % was denoted NPC. The NC with increased N content up to 9 atom % was prepared by the pyrolysis of ZIF-8 powders at 900

4.2. scCO₂-Assisted Synthesis. For Pt₁/NPC synthesis, 60 mg of NPC powders, 5 mg of Pt(acac)2, and 1.5 mL of tetrahydrofuran (THF) were loaded into a glass cell and then placed into an autoclave (volume capacity: 50 mL) located on a heater. THF was used to modify the polarity of CO_2 to dissolve the $Pt(acac)_2$ molecules. The autoclave was heated to 60 °C and 10 MPa of CO₂ was pumped into the autoclave. After stirring for 12 h with a speed of 200 rpm, the autoclave was cooled down to 50 °C and then vented out the CO2 slowly. The collected powders, labeled as Pt(acac)2/NPC were treated with 10 vol % H₂/Ar for 2 h at 200 °C with a heating rate of 2 °C min⁻¹.

4.3. Wet Impregnation Method. 60 mg of NPC was dispersed in 50 mL of THF solvent under sonication for 2 h. 5 mL of Pt(acac)₂ THF solution (1 mg mL⁻¹) was added dropwise into NPC solution under sonication. The suspension was stirred vigorously for 12 h, and the solvent was removed by rotary evaporation. The resulting powder was thermally treated using the same conditions of Pt₁/NPC. The sample was denoted as Pt NPs/NPC.

- 4.4. Physical Characterizations. SEM images were recorded on an FEI Nova Nano 450 with a voltage of 5 kV. TEM and HRTEM images, together with element mapping images, were acquired on a JEOL JEM 2100F working at 200 kV. HAADF-STEM images were performed on FEI Theims Z had an accelerating voltage of 200 kV. XRD analysis was performed on a Bruker D8 Advance diffractometer with Cu-K α (λ = 1.5405 Å) with a scan rate of 0.1° min⁻¹. The surface chemical state of Pt in the samples was analyzed by XPS conducted on a Thermo Scientific Nexsa. The BET surface areas of the samples were measured by N_2 sorption isotherms (77 K) with an ASAP 2020. The pore size distributions were calculated by fitting the full isotherm with the quench solid density functional theory model with slit pore geometry from NovaWin (Quantachrome Instruments). The metal loading was determined by an Agilent ICP-OES system. XAS measurements were performed in transmission or fluorescence mode at the beamline 1W1B station of the Beijing Synchrotron Radiation Facility operated at 2.5 GeV and 250 mA. The XAS data were processed and fitted using the IFEFFIT package. The raw data were background-subtracted, normalized, and Fourier-transformed by the ATHENA program.
- 4.5. Heck Reaction Catalytic Performance. Heck reactions were carried out under a N2 atmosphere in oven-dried Schlenk tubes. Reaction temperatures are reported as the temperature of the heat transfer medium surrounding the vessel unless otherwise stated. Unless otherwise noted, the reaction was carried out as follows: An oven-dried 25 mL Schlenk tube equipped with a stirrer bar was charged with catalyst (1 mol %, relative to substrate), and then halobenzene 1 (0.2 mmol), acrylate 2 (0.26 mmol), and KOAc (0.3 mmol) were added into the reaction mixture with DMF (0.5 mL). The mixture was stirred at 125 $^{\circ}\text{C}$ for 24 h under a N_2 atmosphere. The reaction mixture was then cooled to room temperature. The solvent was evaporated, and the residue was subjected to silica gel column chromatography to give the desired product 3. To demonstrate the potential industrial value, we have conducted largescale experiments for a 20 mmol system with catalyst (0.5 mol %) under the standard reaction condition (halobenzene 1 (20 mmol), acrylate 2 (26 mmol), and KOAc (30 mmol) were added into the reaction mixture with DMF (50 mL)).
- **4.6. Structure Characterization of Product 3.** NMR spectra were recorded on a Bruker AV 400 spectrometer at 400 MHz (1 H NMR) and 100 MHz (13 C NMR). Chemical shifts (δ) for 1 H and 13 C NMR spectra are given in ppm relative to tetramethylsilane (TMS). The residual solvent signals were used as references for 1 H and 13 C NMR spectra, and the chemical shifts were converted to the TMS scale (CDCl₃: δ H = 7.26 ppm, δ C = 77.16 ppm). 1 H and 13 C multiplicities are reported as follows: singlet (s), doublet (d), triplet (t), quartet (q), doublet of doublets (dd), triplet of quartets (tq), multiplet (m), and broad resonance (br). Products 3 are well-known compounds, so they were characterized by a comparison of NMR data with those reported in the literature: 3a-3b, 51 3c-3d, 52 3e, 53 3f-3g, 54 3h.
- **4.7. Reaction Regents.** Halobenzene 1 and acrylate 2 are commercially available, purchased from J&K, Sigma-Aldrich, Bidepharm, or Energy Chemical. Dry solvents (<50 ppm of H $_2$ O) were purchased from Sigma-Aldrich and stored over molecular sieves under an argon atmosphere and transferred under N $_2$. Thin-layer chromatography was done on precoated silica gel 60 F254 plates (Merck). Silica gel 60H (200–300 mesh) was used for general chromatography.
- **4.8. Computational Methods.** Quantum mechanical calculations were carried out using the ORCA software package⁵⁶ with a $PtC_xN_{4-x}/DV-C_{124}$ flake model where the peripheral dangling bonds were capped by 28 H atoms. For all structure optimization, the Perdew-Burke-Ernzerhof (PBE) approximation⁵⁷ was employed in combination with the def2-SV(P) atom-centered Gaussian basis set.⁵⁸ The resultant structures were verified to be either energy minimum (all positive frequencies) or transition state (a single negative curvature) by vibrational frequency calculations at the same level. Single-point energies were evaluated using the PBE0 global hybrid⁵⁹ with the def2-TZVP basis set,⁵⁸ and the solvation of DMF was

accounted for using the SMD model.⁶⁰ All calculations employed the DFT-D4 London dispersion correction.⁶¹ Free energies were evaluated through the application of the entropic quasi-rigid-rotor-harmonic-oscillator approximation.⁶² Visualizations were carried out in the PyMOL program.⁶³

ASSOCIATED CONTENT

Solution Supporting Information

The Supporting Information is available free of charge at https://pubs.acs.org/doi/10.1021/jacs.3c07851.

Computational results and modeling details; procedure and characterization for the Heck reaction (PDF)

AUTHOR INFORMATION

Corresponding Authors

- Klaus Müllen Max Planck Institute for Polymer Research, 55128 Mainz, Germany; orcid.org/0000-0001-6630-8786; Email: klaus.muellen@mpip-mainz.mpg.de.
- William A. Goddard, III Division of Chemistry and Chemical Engineering, California Institute of Technology, Pasadena, California 91125, United States; ⊚ orcid.org/0000-0003-0097-5716; Email: wag@caltech.edu
- Yazhou Zhou School of Materials Science and Engineering, Jiangsu University, Zhenjiang 212013, China; Max Planck Institute for Polymer Research, 55128 Mainz, Germany; orcid.org/0000-0002-0446-2291; Email: yazhou@ujs.edu.cn

Authors

- Bo Li School of Materials Science and Engineering, Jiangsu University, Zhenjiang 212013, China; Division of Chemistry and Chemical Engineering, California Institute of Technology, Pasadena, California 91125, United States
- Cheng-Wei Ju Max Planck Institute for Polymer Research, 55128 Mainz, Germany; Pritzker School of Molecular Engineering, The University of Chicago, Chicago, Illinois 60637, United States; orcid.org/0000-0002-2250-8548
- Wenlong Wang School of Materials Science and Engineering, Jiangsu University, Zhenjiang 212013, China Yanwei Gu — Max Planck Institute for Polymer Research, 55128 Mainz, Germany; ⊙ orcid.org/0000-0003-1718-5868
- Shuai Chen Max Planck Institute for Polymer Research, 55128 Mainz, Germany
- Yongrui Luo Key Laboratory of Organofluorine Chemistry, Shanghai Institute of Organic Chemistry, Chinese Academy of Sciences, Shanghai 200032, P. R. China
- Haozhe Zhang Pritzker School of Molecular Engineering, The University of Chicago, Chicago, Illinois 60637, United States
- Juan Yang School of Materials Science and Engineering, Jiangsu University, Zhenjiang 212013, China; orcid.org/ 0000-0003-0118-7084
- Hai-wei Liang Hefei National Laboratory for Physical Sciences at the Microscale, Department of Chemistry, University of Science and Technology of China, Hefei 230026, China; orcid.org/0000-0002-0128-0222
- Mischa Bonn Max Planck Institute for Polymer Research, 55128 Mainz, Germany; orcid.org/0000-0001-6851-8453

Complete contact information is available at: https://pubs.acs.org/10.1021/jacs.3c07851

Author Contributions

 $^{
abla}$ B.L., C.-W.J., and W.W. contributed equally to this work.

Notes

The authors declare no competing financial interest.

ACKNOWLEDGMENTS

The authors thank the financial support from the Max Planck Society. Y.-Z.Z. and J.Y. thank the Natural Science Foundation of China (51702129 and 51972150). Y.-Z.Z. acknowledges the support from the Postdoctoral Science Foundation (2018M630527), and China Scholarship Council (201708320150). M.B. and Y.-Z.Z. thank the DFG (514772236). B.L. acknowledges the graduate research funding from Caltech. The authors thank Dr. Zehua Wu and Dr. Hao Wu for catalytic performance evolution. W.A.G. and B.L. thank the US National Science Foundation (CBET 2311117, Program Officer McCabe) for support.

REFERENCES

- (1) Wang, A.; Li, J.; Zhang, T. Heterogeneous Single-Atom Catalysis. *Nat. Rev. Chem.* **2018**, 2 (6), 65–81.
- (2) Kaiser, S. K.; Chen, Z.; Akl, D. F.; Mitchell, S.; Pérez-Ramírez, J. Single-Atom Catalysts across the Periodic Table. *Chem. Rev.* **2020**, 120 (21), 11703–11809, DOI: 10.1021/acs.chemrev.0c00576.
- (3) Li, Z.; Chen, Y.; Ji, S.; Tang, Y.; Chen, W.; Li, A.; Zhao, J.; Xiong, Y.; Wu, Y.; Gong, Y.; Yao, T.; Liu, W.; Zheng, L.; Dong, J.; Wang, Y.; Zhuang, Z.; Xing, W.; He, C.-T.; Peng, C.; Cheong, W.-C.; Li, Q.; Zhang, M.; Chen, Z.; Fu, N.; Gao, X.; Zhu, W.; Wan, J.; Zhang, J.; Gu, L.; Wei, S.; Hu, P.; Luo, J.; Li, J.; Chen, C.; Peng, Q.; Duan, X.; Huang, Y.; Chen, X.-M.; Wang, D.; Li, Y. Iridium Single-Atom Catalyst on Nitrogen-Doped Carbon for Formic Acid Oxidation Synthesized Using a General Host—Guest Strategy. *Nat. Chem.* 2020, 12 (8), 764—772.
- (4) Cheng, N.; Zhang, L.; Doyle-Davis, K.; Sun, X. Single-Atom Catalysts: From Design to Application. *Electrochem. Energy Rev.* **2019**, 2 (4), 539–573.
- (5) Qiao, B.; Wang, A.; Yang, X.; Allard, L. F.; Jiang, Z.; Cui, Y.; Liu, J.; Li, J.; Zhang, T. Single-Atom Catalysis of CO Oxidation Using Pt1/FeOx. *Nat. Chem.* **2011**, *3* (8), 634–641.
- (6) Giulimondi, V.; Mitchell, S.; Pérez-Ramírez, J. Challenges and Opportunities in Engineering the Electronic Structure of Single-Atom Catalysts. ACS Catal. 2023, 13 (5), 2981–2997.
- (7) Liang, X.; Fu, N.; Yao, S.; Li, Z.; Li, Y. The Progress and Outlook of Metal Single-Atom-Site Catalysis. *J. Am. Chem. Soc.* **2022**, 144 (40), 18155–18174.
- (8) Liu, Q.; Zhang, Z. Platinum Single-Atom Catalysts: A Comparative Review towards Effective Characterization. *Catal. Sci. Technol.* **2019**, 9 (18), 4821–4834.
- (9) Shan, J.; Ye, C.; Jiang, Y.; Jaroniec, M.; Zheng, Y.; Qiao, S.-Z. Metal-Metal Interactions in Correlated Single-Atom Catalysts. *Sci. Adv.* **2022**, 8 (17), No. eabo0762.
- (10) Liu, L.; Corma, A. Metal Catalysts for Heterogeneous Catalysis: From Single Atoms to Nanoclusters and Nanoparticles. *Chem. Rev.* **2018**, *118* (10), 4981–5079.
- (11) Van de Vyver, S.; Román-Leshkov, Y. Metalloenzyme-Like Zeolites as Lewis Acid Catalysts for C-C Bond Formation. *Angew. Chem., Int. Ed.* **2015**, 54 (43), 12554–12561.
- (12) Choi, J.; Fu, G. C. Transition Metal—Catalyzed Alkyl-Alkyl Bond Formation: Another Dimension in Cross-Coupling Chemistry. *Science* **2017**, 356 (6334), No. eaaf7230.
- (13) Wang, S.-S.; Yang, G.-Y. Recent Developments in Low-Cost TM-Catalyzed Heck-Type Reactions (TM = Transition Metal, Ni, Co, Cu, and Fe). *Catal. Sci. Technol.* **2016**, *6* (9), 2862–2876.
- (14) Kurandina, D.; Chuentragool, P.; Gevorgyan, V. Transition-Metal-Catalyzed Alkyl Heck-Type Reactions. *Synthesis* **2019**, *51* (05), 985–1005.

- (15) Grover, J.; Prakash, G.; Goswami, N.; Maiti, D. Traditional and Sustainable Approaches for the Construction of C–C Bonds by Harnessing C–H Arylation. *Nat. Commun.* **2022**, *13* (1), No. 1085.
- (16) Cross-Coupling Reactions: A Practical Guide; Miyaura, N.; de Meijere, A.; Kessler, H.; Ley, S. V.; Thiem, J.; Vögtle, F.; Houk, K. N.; Lehn, J.-M.; Schreiber, S. L.; Trost, B. M.; Yamamoto, H., Eds.; Springer Berlin Heidelberg: Berlin, Heidelberg, 2002; Vol. 219.
- (17) Miyaura, N.; Yamada, K.; Suzuki, A. A New Stereospecific Cross-Coupling by the Palladium-Catalyzed Reaction of 1-Alkenylboranes with 1-Alkenyl or 1-Alkynyl Halides. *Tetrahedron Lett.* **1979**, 20 (36), 3437–3440.
- (18) Heck, R. F.; Nolley, J. P. Palladium-Catalyzed Vinylic Hydrogen Substitution Reactions with Aryl, Benzyl, and Styryl Halides. *J. Org. Chem.* **1972**, 37 (14), 2320–2322.
- (19) Ding, Y.-H.; Fan, H.-X.; Long, J.; Zhang, Q.; Chen, Y. The Application of Heck Reaction in the Synthesis of Guaianolide Sesquiterpene Lactones Derivatives Selectively Inhibiting Resistant Acute Leukemic Cells. *Bioorg. Med. Chem. Lett.* **2013**, 23 (22), 6087–6092.
- (20) Torborg, C.; Beller, M. Recent Applications of Palladium-Catalyzed Coupling Reactions in the Pharmaceutical, Agrochemical, and Fine Chemical Industries. *Adv. Synth. Catal.* **2009**, *351* (18), 3027–3043.
- (21) Karimi, B.; Behzadnia, H.; Elhamifar, D.; Akhavan, P.; Esfahani, F.; Zamani, A. Transition-Metal-Catalyzed Oxidative Heck Reactions. *Synthesis* **2010**, *2010* (09), 1399–1427.
- (22) Zhang, W. Heck Macrocyclization in Natural Product Total Synthesis. *Nat. Prod. Rep.* **2021**, *38* (6), 1109–1135.
- (23) Paul, D.; Das, S.; Saha, S.; Sharma, H.; Goswami, R. K. Intramolecular Heck Reaction in Total Synthesis of Natural Products: An Update. *Eur. J. Org. Chem.* **2021**, *2021* (14), 2057–2076.
- (24) Dounay, A. B.; Overman, L. E. The Asymmetric Intramolecular Heck Reaction in Natural Product Total Synthesis. *Chem. Rev.* **2003**, 103 (8), 2945–2964.
- (25) Epping, R. F. J.; Vesseur, D.; Zhou, M.; De Bruin, B. Carbene Radicals in Transition-Metal-Catalyzed Reactions. *ACS Catal.* **2023**, 13 (8), 5428–5448.
- (26) Liu, Z.; Arnold, F. H. New-to-Nature Chemistry from Old Protein Machinery: Carbene and Nitrene Transferases. *Curr. Opin. Biotechnol.* **2021**, *69*, 43–51.
- (27) Kaur, P.; Tyagi, V. Recent Advances in Iron-Catalyzed Chemical and Enzymatic Carbene-Transfer Reactions. *Adv. Synth. Catal.* **2021**, 363 (4), 877–905.
- (28) Lewis, R. D.; Garcia-Borràs, M.; Chalkley, M. J.; Buller, A. R.; Houk, K. N.; Kan, S. B. J.; Arnold, F. H. Catalytic Iron-Carbene Intermediate Revealed in a Cytochrome *c* Carbene Transferase. *Proc. Natl. Acad. Sci. U.S.A.* **2018**, *115* (28), 7308–7313.
- (29) Chen, Z.; Vorobyeva, E.; Mitchell, S.; Fako, E.; Ortuño, M. A.; López, N.; Collins, S. M.; Midgley, P. A.; Richard, S.; Vilé, G.; Pérez-Ramírez, J. A Heterogeneous Single-Atom Palladium Catalyst Surpassing Homogeneous Systems for Suzuki Coupling. *Nat. Nanotechnol.* **2018**, *13* (8), 702–707.
- (30) Zhang, X.; Sun, Z.; Wang, B.; Tang, Y.; Nguyen, L.; Li, Y.; Tao, F. F. C-C Coupling on Single-Atom-Based Heterogeneous Catalyst. *J. Am. Chem. Soc.* **2018**, *140* (3), 954–962.
- (31) Zhao, J.; Ji, S.; Guo, C.; Li, H.; Dong, J.; Guo, P.; Wang, D.; Li, Y.; Toste, F. D. A Heterogeneous Iridium Single-Atom-Site Catalyst for Highly Regioselective Carbenoid O–H Bond Insertion. *Nat. Catal.* **2021**, *4* (6), 523–531.
- (32) Chen, Y.; Ji, S.; Chen, C.; Peng, Q.; Wang, D.; Li, Y. Single-Atom Catalysts: Synthetic Strategies and Electrochemical Applications. *Joule* **2018**, 2 (7), 1242–1264.
- (33) Sun, X.; Dawson, S. R.; Parmentier, T. E.; Malta, G.; Davies, T. E.; He, Q.; Lu, L.; Morgan, D. J.; Carthey, N.; Johnston, P.; Kondrat, S. A.; Freakley, S. J.; Kiely, C. J.; Hutchings, G. J. Facile Synthesis of Precious-Metal Single-Site Catalysts Using Organic Solvents. *Nat. Chem.* **2020**, *12* (6), 560–567.
- (34) Wang, L.; Chen, M.-X.; Yan, Q.-Q.; Xu, S.-L.; Chu, S.-Q.; Chen, P.; Lin, Y.; Liang, H.-W. A Sulfur-Tethering Synthesis Strategy

- toward High-Loading Atomically Dispersed Noble Metal Catalysts. Sci. Adv. 2019, 5 (10), No. eaax6322.
- (35) Li, J.; Chen, C.; Xu, L.; Zhang, Y.; Wei, W.; Zhao, E.; Wu, Y.; Chen, C. Challenges and Perspectives of Single-Atom-Based Catalysts for Electrochemical Reactions. *JACS Au* **2023**, *3* (3), 736–755.
- (36) Pai, R. A.; Humayun, R.; Schulberg, M. T.; Sengupta, A.; Sun, J.-N.; Watkins, J. J. Mesoporous Silicates Prepared Using Preorganized Templates in Supercritical Fluids. *Science* **2004**, *303* (5657), 507–510.
- (37) Zhou, Y.; Yen, C. H.; Hu, Y. H.; Wang, C.; Cheng, X.; Wai, C. M.; Yang, J.; Lin, Y. Making Ultrafine and Highly-Dispersive Multimetallic Nanoparticles in Three-Dimensional Graphene with Supercritical Fluid as Excellent Electrocatalyst for Oxygen Reduction Reaction. J. Mater. Chem. A 2016, 4 (47), 18628–18638.
- (38) Gao, S.; Yang, H.; Rao, D.; Wang, N.; Li, Y.; Li, J.; Rao, S.; Maouche, C.; Wu, Z.; Li, B.; Zhou, Y.; Yang, J. Supercritical CO2 Assisted Synthesis of Highly Accessible Iron Single Atoms and Clusters on Nitrogen-Doped Carbon as Efficient Oxygen Reduction Electrocatalysts. *Chem. Eng. J.* 2022, 433, No. 134460.
- (39) Zhou, Y.; Cheng, X.; Yen, C. H.; Wai, C. M.; Wang, C.; Yang, J.; Lin, Y. Synthesis of an Excellent Electrocatalyst for Oxygen Reduction Reaction with Supercritical Fluid: Graphene Cellular Monolith with Ultrafine and Highly Dispersive Multimetallic Nanoparticles. *J. Power Sources* **2017**, 347, 69–78.
- (40) Zhou, Y.; Lu, R.; Tao, X.; Qiu, Z.; Chen, G.; Yang, J.; Zhao, Y.; Feng, X.; Müllen, K. Boosting Oxygen Electrocatalytic Activity of Fe–N–C Catalysts by Phosphorus Incorporation. *J. Am. Chem. Soc.* **2023**, 145 (6), 3647–3655.
- (41) Zhou, Y.; Tao, X.; Chen, G.; Lu, R.; Wang, D.; Chen, M.-X.; Jin, E.; Yang, J.; Liang, H.-W.; Zhao, Y.; Feng, X.; Narita, A.; Müllen, K. Multilayer Stabilization for Fabricating High-Loading Single-Atom Catalysts. *Nat. Commun.* **2020**, *11* (1), No. 5892.
- (42) Wood, K. N.; O'Hayre, R.; Pylypenko, S. Recent Progress on Nitrogen/Carbon Structures Designed for Use in Energy and Sustainability Applications. *Energy Environ. Sci.* **2014**, 7 (4), 1212–1249.
- (43) Hirshfeld, F. L. Bonded-Atom Fragments for Describing Molecular Charge Densities. *Theoret. Chim. Acta* 1977, 44 (2), 129–138
- (44) Bickelhaupt, F. M.; Houk, K. N. Analyzing Reaction Rates with the Distortion/Interaction-Activation Strain Model. *Angew. Chem., Int. Ed.* **2017**, *56* (34), 10070–10086.
- (45) Knizia, G. Intrinsic Atomic Orbitals: An Unbiased Bridge between Quantum Theory and Chemical Concepts. *J. Chem. Theory Comput.* **2013**, *9* (11), 4834–4843.
- (46) Knizia, G.; Klein, J. E. M. N. Electron Flow in Reaction Mechanisms-Revealed from First Principles. *Angew. Chem., Int. Ed.* **2015**, 54 (18), 5518–5522.
- (47) Li, L.; Chang, X.; Lin, X.; Zhao, Z.-J.; Gong, J. Theoretical Insights into Single-Atom Catalysts. *Chem. Soc. Rev.* **2020**, 49 (22), 8156–8178.
- (48) Yang, J.; Liu, W.; Xu, M.; Liu, X.; Qi, H.; Zhang, L.; Yang, X.; Niu, S.; Zhou, D.; Liu, Y.; Su, Y.; Li, J.-F.; Tian, Z.-Q.; Zhou, W.; Wang, A.; Zhang, T. Dynamic Behavior of Single-Atom Catalysts in Electrocatalysis: Identification of Cu-N 3 as an Active Site for the Oxygen Reduction Reaction. *J. Am. Chem. Soc.* **2021**, *143* (36), 14530–14539.
- (49) Tang, Y.; Asokan, C.; Xu, M.; Graham, G. W.; Pan, X.; Christopher, P.; Li, J.; Sautet, P. Rh Single Atoms on TiO2 Dynamically Respond to Reaction Conditions by Adapting Their Site. *Nat. Commun.* **2019**, *10* (1), No. 4488.
- (50) Zhang, W.; Fu, Q.; Luo, Q.; Sheng, L.; Yang, J. Understanding Single-Atom Catalysis in View of Theory. *JACS Au* **2021**, *1* (12), 2130–2145.
- (51) Zhang, H.; Huang, X. Ligand-Free Heck Reactions of Aryl Iodides: Significant Acceleration of the Rate through Visible Light Irradiation at Ambient Temperature. *Adv. Synth. Catal.* **2016**, 358 (23), 3736–3742.

- (52) Li, Y.; Liu, G.; Cao, C.; Wang, S.; Li, Y.; Pang, G.; Shi, Y. Controlled Mono- and Double-Heck Reaction Catalyzed by a Dicarbene Dipalladium Complex. *Tetrahedron* **2013**, *69* (30), 6241–6250.
- (53) Fan, J.; Dai, Y.; Shao, J.; Peng, X.; Wang, C.; Cao, S.; Zhao, B.; Ai, J.; Geng, M.; Duan, W. Design, Synthesis and Biological Evaluation of Pyrazolylaminoquinazoline Derivatives as Highly Potent Pan-Fibroblast Growth Factor Receptor Inhibitors. *Bioorg. Med. Chem. Lett.* **2016**, 26 (11), 2594–2599.
- (54) Valentini, F.; Ferlin, F.; Lilli, S.; Marrocchi, A.; Ping, L.; Gu, Y.; Vaccaro, L. Valorisation of Urban Waste to Access Low-Cost Heterogeneous Palladium Catalysts for Cross-Coupling Reactions in Biomass-Derived γ-Valerolactone. *Green Chem.* **2021**, 23 (16), 5887–5895.
- (55) Selvakumar, K.; Zapf, A.; Beller, M. New Palladium Carbene Catalysts for the Heck Reaction of Aryl Chlorides in Ionic Liquids. *Org. Lett.* **2002**, *4* (18), 3031–3033.
- (56) Neese, F. The ORCA Program System. WIREs Comput. Mol. Sci. 2012, 2 (1), 73-78.
- (57) Perdew, J. P.; Burke, K.; Ernzerhof, M. Generalized Gradient Approximation Made Simple. *Phys. Rev. Lett.* **1996**, 77 (18), 3865–3868.
- (58) Weigend, F.; Ahlrichs, R. Balanced Basis Sets of Split Valence, Triple Zeta Valence and Quadruple Zeta Valence Quality for H to Rn: Design and Assessment of Accuracy. *Phys. Chem. Chem. Phys.* **2005**, 7 (18), 3297–3305, DOI: 10.1039/b508541a.
- (59) Adamo, C.; Barone, V. Toward Reliable Density Functional Methods without Adjustable Parameters: The PBE0Model. *J. Chem. Phys.* **1999**, *110* (13), 6158–6170.
- (60) Marenich, A. V.; Cramer, C. J.; Truhlar, D. G. Universal Solvation Model Based on Solute Electron Density and on a Continuum Model of the Solvent Defined by the Bulk Dielectric Constant and Atomic Surface Tensions. *J. Phys. Chem. B* **2009**, *113* (18), 6378–6396.
- (61) Caldeweyher, E.; Ehlert, S.; Hansen, A.; Neugebauer, H.; Spicher, S.; Bannwarth, C.; Grimme, S. A Generally Applicable Atomic-Charge Dependent London Dispersion Correction. *J. Chem. Phys.* **2019**, *150* (15), No. 154122.
- (62) Grimme, S. Supramolecular Binding Thermodynamics by Dispersion-Corrected Density Functional Theory. *Chem. Eur. J.* **2012**, *18* (32), 9955–9964.
- (63) Delano, W. The PyMOL Molecular Graphics System, Version 2.6.0a0; Schrodinger, LLC., 2010.